Available online at www.sciencedirect.com
ScienceDirect
International Journal of Heat and Mass Transfer 50 (2007) 1656–1667
International Journal of HEAT and MASS TRANSFER
www.elsevier.com/locate/ijhmt

Solidification of a ternary alloy liquid layer on a substrate subject to self-consistent melting

F.B. Yeh *

Department of Marine Mechanical Engineering, Chinese Naval Academy, P.O. Box 90175, Tsoying, Kaohsiung, Taiwan, ROC

Received 18 January 2006; received in revised form 21 October 2006
Available online 15 December 2006

Abstract

Micro-electro-mechanical (MEMS), plasma or powder spray deposition, surface coating, semiconductor technology, splat cooling, single and twin-roller melt-spinning, strip and slab casting, melt-extraction, etc. are usually characterized by solidification of a thin liquid layer on a cold substrate. A one-dimensional model of enthalpy formation of the energy and species conservation equations with thermodynamic relationships from ternary equilibrium diagram are solved to study the solidification processes for ternary alloys molten liquid layer on the ternary eutectic solid substrate. The solidification path of the liquid layer may pass through the primary, cotectic and eutectic solidification regions. The melting and re-solidification of the substrate happens at the ternary eutectic point. The thermal physical properties of the splat and substrate are identical and imperfect contact of contact surface between the splat and substrate is considered. The temperature functions as compositions are assumed as linear along the liquidus surface and cotectic curves. The temperature distributions of the solidified splat and the melted, re-solidified substrate, the thicknesses of the different mushy layers of splat and melting of substrate subject to different process parameters and thermal physical properties are quantitatively and extensively investigated. The initiation times for primary, cotectic mushy and eutectic solid fronts of splat and the complete re-solidification times of the substrate are affected by different parameters, these are also investigated. Results of this study are compared with experimental data provided by Aitta et al. The growth rates of the cotectic and eutectic fronts are found to agree well with experimental data. The effects of initial solute concentrations of liquid layer, solute concentrations and temperatures at the binary and ternary eutectic points on the thicknesses of different mushy layers are important and presented.

Keywords: Ternary alloys; Eutectic solidification; Ternary phase diagram; Mushy

1. Introduction

Solidification of a thin liquid layer on a cold substrate usually happens in different metal manufacturing processes, such as plasma or powder spray deposition, surface coating, MEMS, semiconductor technology, splat cooling, single and twin-roller melt-spinning, strip and slab casting, melt-extraction, etc. Solidification material may be a pure metal or a multiconstituent alloy. Multiconstituent alloys are extensively applied in many manufacturing processes, resulting from significantly improvement in metallurgical technology and the solidification qualities of multiconstituent alloys. Melting and solidification of multiconstituent systems, unlike that of pure substance, are characterized by the existence of a multiphase (or mushy region). It is this region that separates the pure solid and liquid regions of the domain. The primary difficulty encountered when dealing with multiconstituent phase change is that such phases do not, in general, coexist in equilibrium phase temperature within the multiphase region. This is can be attributed to the differences in solubilities of constituents within each phase, constituents are selectively rejected or incorporated at microscopic interface within the mushy region and phase compositions are often vastly different [1,2].

* Tel./fax: +886 7 5834861.
E-mail address: fbyeh@mail.cna.edu.tw

0017-9310/$ - see front matter © 2006 Elsevier Ltd. All rights reserved.
doi:10.1016/j.ijheatmasstransfer.2006.10.023

Nomenclature

Bi	Biot number; $Bi_{2,\infty} = h_{2,\infty}s/k_\ell$, $Bi_c = h_c s/k_\ell$
c_p	specific heat
$C_{ps\ell}$	specific heat ratio; $C_{ps\ell} = c_{ps}/c_{p\ell}$
d	substrate thickness
D	dimension and dimensionless solute diffusivity, $D_m = D_m/D_\ell^A$
f	mass fraction
f^A	dimension and dimensionless A solute mass fraction, $f_m^A = f_m^A/f_{1,m,0}^A$, $f_\ell^A = f_\ell^A/f_{1,m,0}^A$, $f_\alpha^A = f_\alpha^A/f_{1,m,0}^A$, $f_\beta^A = f_\beta^A/f_{1,m,0}^A$, $f_\delta^A = f_\delta^A/f_{1,m,0}^A$
f^B	dimension and dimensionless B solute mass fraction, $f_m^B = f_m^B/f_{1,m,0}^A$, $f_\ell^B = f_\ell^B/f_{1,m,0}^A$, $f_\alpha^B = f_\alpha^B/f_{1,m,0}^A$, $f_\beta^B = f_\beta^B/f_{1,m,0}^A$, $f_\delta^B = f_\delta^B/f_{1,m,0}^A$
$f_{i,m,0}^j$	dimension and dimensionless initial solute content, $f_{1,m,0}^B = f_{1,m,0}^B/f_{1,m,0}^A$, $f_{2,m,0}^A = f_{2,m,0}^A/f_{1,m,0}^A$, $f_{2,m,0}^B = f_{2,m,0}^B/f_{1,m,0}^A$
h	dimension enthalpy
h_f	latent heat of fusion at ternary eutectic point
k, K	dimension and dimensionless thermal conductivity, $K_m = K_m/k_\ell$
$K_{s\ell}$	solid-to-liquid thermal conductivity ratio, $K_{s\ell} = k_s/k_\ell$
k_α, k_β, k_δ	equilibrium partition coefficient
Le	Lewis number, $Le = \alpha_\ell/D_\ell^A$
m_ℓ^A, m_ℓ^B	dimensionless liquidus line slopes of solute A and B at the liquidus surface, respectively
m_c^A, m_c^B	dimensionless cotectic line slopes of solute A and B, respectively
s	thickness of molten liquid layer
S	dimensionless thickness of substrate, $S = d/s$
Ste	Stefan number, $Ste = c_{p\ell}T_\infty/h_f$
T	dimension temperature
t	time
x	Cartesian coordinate

Greek symbols

ξ	dimensionless coordinate, $\xi = x/s$
λ	dimensionless enthalpy, $\lambda_m = h_m/h_f$
θ	dimensionless temperature, $\theta = T/T_\infty$
Λ	functions, defined in Eqs. (33), (34), (38) and (39)
ρ	density
τ	dimensionless time, $\tau = tD_\ell^A/s^2$

Superscripts

A, B, C solute

Subscripts

α, β, δ	solid phase
be	binary eutectic point at the solute C and A side
cp	cotectic point
i	splat or substrate
ℓ	liquid
ℓiq	liquidus
m	mixture or melting
s	solid
soℓ	solidus
te	ternary eutectic point
1, 2	splat and substrate, respectively
0	initial condition or coordinate origin at $\xi = 0$ as shown in Fig. 1

Several models have been developed to simulate the solidification and melting of a binary alloy, from analytical expressions [3–5] to numerical simulations [6–11]. Under the assumption of local equilibrium at the interface, Coriell et al. [3] explored the multiple similarity solutions to find the analytical expressions to the transport equations for heat and solute in one spatial dimension during the solidification or melting of a binary alloy. A fully analytical solution for solid, liquid and mushy regions was proposed by Chakraborty and Dutta [5] to simulate the transient, one-dimensional, conduction-dominated alloy solidification. Krane and Incropera [6] applied the scaling analysis to the conservation equations for momentum, heat and species transport, the full continuum mixture model derived by Bennon and Incropera [7], to examine a bottom cooled binary alloy. Results show that several terms in the momentum equation can be neglected throughout the solidifying domain. Ganaoui et al. [8] proposed a computational model to investigate the time-dependent behaviors induced by solutal convection in the melt for directional solidification of a binary alloy and studied effects of solutal Rayleigh number on flow, heat and mass transfer. A comparative assessment of the finite volume and finite element methods is performed by Celentano et al. [9] in the analysis of solidification in mould cavities involving natural convection. Results show that both methodologies provided equivalent results in the described application, but some small discrepancies existed for high Rayleigh numbers.

More recently, a number of notable attempts to predict the solidification behavior of multicomponent alloys have reported, which includes analytical solutions [12–16], numerical simulations [17–21] and the experimental study [22–24]. Most are formulated as extensions of the binary models with additional equation to solve the additional phase fractions and composition variables. An analytical solution requires a simplified multicomponent phase diagram for a multicomponent system. The first analytical study of macrosegregation during the solidification of a multicomponent alloy Al–Cu–Ni was performed by Mehrabian and Flemings [12]. Voller [14] proposed a

semi-analytical similarity solution for a multicomponent solidification. A simplified model for microsegregation in multicomponent system was proposed by Cefalu and Krane [15] to simulate the solidification, remelting, and dissolution of solid that may occur due to thermal and solutal changes. Schneider and Beckermann [17] expanded the continuum formulation derived by Beckermann and Viskanta [18] to calculate macrosegregation in a multicomponent system. Krane and Incropera [20] constructed a model to simulate the solidification of the ternary alloy based on previous treatments of transport phenomena for the binary alloy solidification [7]. The continuum mixture equations for the transport of mass, momentum, energy and species for the three components of the ternary alloy with the thermodynamic relations from the ternary equilibrium phase diagram to simulate the ternary alloy solidification that includes primary solid phase, binary eutectic troughs, ternary eutectic and peritectic reactions, and the formation of an intermetallic compound [21].

Aitta et al. [23] presented an experimental study of the ternary alloy H_2O–KNO_3–$NaNO_3$ solidification from a cooled boundary. The solidification front growth was diffusion-controlled under their experimental operation, however the convection effects due to thermal and solutal buoyancy are absent. There are two distinguishable mushy layers (named primary and cotectic mushy) that exist between the liquid layer and a eutectic solid layer during ternary alloy solidification. The locations of the various mushy fronts are estimated from measurements of the concentration and temperature fields, the corresponding thicknesses all grow in proportion to the square root of time under diffusion-limited growth are confirmed, and the constants of proportionality are determined. Accordingly the above work [23], Anderson [16] proposed a diffusion-controlled model incorporating a ternary phase diagram for one-dimensional solidification of a ternary alloy that includes various mushy layers formation. The temperature, solute and solid fraction distribution with each mushy layer are obtained from a one-dimensional similarity solution and investigate numerically the role of the control parameters in the growth characteristics. These results show that the thicknesses of the primary mushy, cotectic mushy and eutectic layer depend strongly on the initial compositions of the ternary alloy.

Whether a deposited melt may induce melting of the substrate or not is important in many manufacturing processes, such as spray deposition, microcasting, coating and similar processes involving the deposition of metal droplets on a substrate or previously deposited layer. In addition to mechanical attachment of the coating layer on the substrate, a strong bond between the coating and substrate can also be formed through substrate melting. An understanding of the substrate melting after deposition is, therefore, essential to achieve good control of the bonding between the layers [25–32]. Steffens et al. [26] explained the tensile strength measurements of the coatings, this indicated that a higher interface temperature above the melting temperature of the substrate usually led to a better bonding between the coating and substrate. Kang et al. [28] numerically investigated a tin droplet impacting on a substrate, and later impacted itself by a second droplet. Wang et al. [29] generated operational maps to predict whether melting of the substrate will take place before freezing of the splat. Li et al. [30] numerically and experimentally investigated the droplet solidification, melting and re-solidification phenomenon of the substrate during thermal spray. Yeh et al. [31,32] studied the effects of different thermal and physical properties, kinetic condition, external heat extraction and imperfect contact between the splat and substrate on the rapid solidification of a thin molten splat on a cold substrate experiencing self-consistent solidification and melting. The materials are studied in the above work had been restricted to pure metal or binary alloy, investigating the molten ternary alloy splat on the ternary alloy solid substrate experiencing self-consistent solidification and melting, re-solidification is incomplete.

In this work, the continuum formulations are based on the enthalpy method for one-dimensional energy and species conservation equations [20]. These are used to solve the enthalpy and species mass fraction distributions in the molten liquid layer and substrate. The objective of this work is to study the effects of process parameters and thermal physical properties of liquid layer and substrate on the solidification of splat, with the melting and re-solidification of substrate. The imperfect contact between the splat and substrate experiencing self-consistent solidification and melting, re-solidification are considered.

2. System model and analysis

As illustrated in Fig. 1, this work is to investigate heat and species transport of a molten ternary alloy splat in a thin layer of a thickness s at an initial temperature $T_{1,0}$ contact with a cold ternary alloy substrate of a thickness d initially at a temperature $T_{2,0}$. The splat undergoes a freezing,

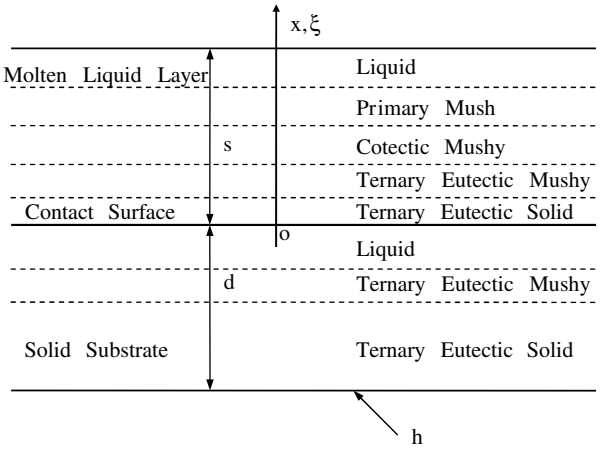

Fig. 1. Physical model and coordinate system.

from liquid experiences primary, cotectic and ternary eutectic mushy to ternary eutectic solid, while the substrate experiences heating or possible melting from ternary eutectic solid through ternary eutectic mushy to liquid at the eutectic temperature then re-solidified.

2.1. Basic assumptions and consideration

1. Local thermodynamic equilibrium.
2. Phase specific heats are assumed constant.
3. Negligible species diffusion in the solid phase.
4. Saturated mixture condition.
5. The relationships between temperature and composition along the liquidus surface and cotectic curves are linear.
6. Unsteady heat and species transport equations are one-dimensional as a result of thin thickness of the splat much smaller than its radius of curvature.
7. Fluid flow is ignored, the solidification process is conduction dominated.
8. Chemical reactions or intermetallic compounds between the splat and substrate are neglected.
9. The thermal physical properties for the thin molten splat and substrate are identical. The properties of solid and liquid are distinct except for the density. The properties of the different precipitated α, β and δ solid phases are same.

2.2. Governing equations

The enthalpy formation of the energy and species conservation equations for splat and substrate are, respectively [20]

$$\frac{\partial \lambda_{i,\mathrm{m}}}{\partial \tau} = \frac{Le}{C_{ps\ell}} \left\{ \frac{\partial}{\partial \xi} \left(K_{i,\mathrm{m}} \frac{\partial \lambda_{i,\mathrm{m}}}{\partial \xi} \right) + \frac{\partial}{\partial \xi} \left[K_{i,\mathrm{m}} \frac{\partial}{\partial \xi} (\lambda_{i,\mathrm{s}} - \lambda_{i,\mathrm{m}}) \right] \right\} \tag{1}$$

$$\frac{\partial f^j_{i,\mathrm{m}}}{\partial \tau} = \frac{\partial}{\partial \xi} \left(D_{i,\mathrm{m}} \frac{\partial f^j_{i,\mathrm{m}}}{\partial \xi} \right) + \frac{\partial}{\partial \xi} \left[D_{i,\mathrm{m}} \frac{\partial}{\partial \xi} (f^j_{i,\ell} - f^j_{i,\mathrm{m}}) \right] \tag{2}$$

where $\lambda_{i,\mathrm{m}}$ and $f^j_{i,\mathrm{m}}$ denote the dimensionless enthalpy and solute mass fraction, respectively. $\lambda_{i,\mathrm{s}} = SteC_{ps\ell}\theta_i$, $Ste = c_{p\ell}T_\infty/h_\mathrm{f}$, $\theta_i = T_i/T_\infty$. The subscript i is 1 and 2 represents the splat and substrate, respectively, and the superscript j denotes the component A and B. Mass conservation requires $f^\mathrm{A}_{i,\mathrm{m}} + f^\mathrm{B}_{i,\mathrm{m}} + f^\mathrm{C}_{i,\mathrm{m}} = 1$, so a mixture species conservation equation for $f^\mathrm{C}_{i,\mathrm{m}}$ is not necessary. The dimensionless independent variables as follow:

$$Le = \frac{\alpha_\ell}{D^\mathrm{A}_\ell}, \quad C_{ps\ell} = \frac{c_{ps}}{c_{p\ell}} \tag{3}$$

The dimensionless mixture thermal conductivity, mass diffusion coefficient are defined as

$$K_{i,\mathrm{m}} = f_{i,\mathrm{s}}K_{\mathrm{s}\ell} + f_{i,\ell}, \quad D_{i,\mathrm{m}} = f_{i,\ell} \tag{4}$$

where $K_{\mathrm{s}\ell} = k_\mathrm{s}/k_\ell$.

2.3. Initial and boundary conditions

The initial and boundary conditions for the molten splat and solid substrate are

$$\lambda_{1,\mathrm{m}} = Ste\theta_{1,0} + \lambda^0_\ell, \quad f_{1,\mathrm{s}} = 0, \quad f_{1,\ell} = 1, \quad f^\mathrm{A}_{1,\mathrm{m}} = 1$$
$$f^\mathrm{B}_{1,\mathrm{m}} = f^\mathrm{B}_{1,\mathrm{m},0}, \quad \tau = 0, \quad 0 \leqslant \xi \leqslant 1 \tag{5}$$

$$\lambda_{2,\mathrm{m}} = C_{ps\ell}Ste\theta_{2,0}, \quad f_{2,\mathrm{s}} = 1, \quad f_{2,\ell} = 0, \quad f^\mathrm{A}_{2,\mathrm{m}} = f^\mathrm{A}_{2,\mathrm{m},0}$$
$$f^\mathrm{B}_{2,\mathrm{m}} = f^\mathrm{B}_{2,\mathrm{m},0}, \quad \tau = 0, \quad -S \leqslant \xi \leqslant 0 \tag{6}$$

$$\frac{\partial \lambda_{1,\mathrm{m}}}{\partial \xi} = 0, \quad \frac{\partial f^j_{1,\mathrm{m}}}{\partial \xi} = 0, \quad \xi = 1 \tag{7}$$

$$K_{2,\mathrm{m}} \frac{\partial \lambda_{2,\mathrm{m}}}{\partial \xi} = Bi_{2,\infty}(\lambda_{2,\mathrm{m}} - SteC_{ps\ell}), \quad \frac{\partial f^j_{2,\mathrm{m}}}{\partial \xi} = 0, \quad \xi = -S \tag{8}$$

$$K_{1,\mathrm{m}} \frac{\partial \lambda_{1,\mathrm{m}}}{\partial \xi} = K_{2,\mathrm{m}} \frac{\partial \lambda_{2,\mathrm{m}}}{\partial \xi},$$
$$K_{1,\mathrm{m}} \frac{\partial \lambda_{1,\mathrm{m}}}{\partial \xi} = Bi_\mathrm{c}(\lambda_{1,\mathrm{m}} - \lambda_{2,\mathrm{m}}), \quad \xi = 0 \tag{9}$$

$$\frac{\partial f^j_{1,\mathrm{m}}}{\partial \xi} = 0, \quad \frac{\partial f^j_{2,\mathrm{m}}}{\partial \xi} = 0, \quad \xi = 0 \tag{10}$$

where $\lambda^0_\ell = Ste(C_{ps\ell} - 1)\theta_{\mathrm{so}\ell} + 1$, $\theta_{\mathrm{so}\ell}$ denotes the solidus temperature. $f^\mathrm{B}_{1,\mathrm{m},0}$, $f^\mathrm{A}_{2,\mathrm{m},0}$ and $f^\mathrm{B}_{2,\mathrm{m},0}$ denote the initial contents of B solute in splat, A and B solutes in substrate, respectively. $Bi_{2,\infty} = h_{2,\infty}s/k_\ell$, $Bi_\mathrm{c} = h_\mathrm{c}s/k_\ell$ is contact Biot numbers, the h_c is contact heat transfer coefficient. Conservation of energy at the contact surface between the splat and substrate is satisfied by Eq. (9), which governs the discontinuity of temperatures across the contact surface.

2.4. The ternary phase diagram

A top view of an idealized ternary phase diagram for the elements A, B and C with temperature as the axial coordinate and composition represents on the base is shown in Fig. 2. Here the liquidus point indicates that the liquidus

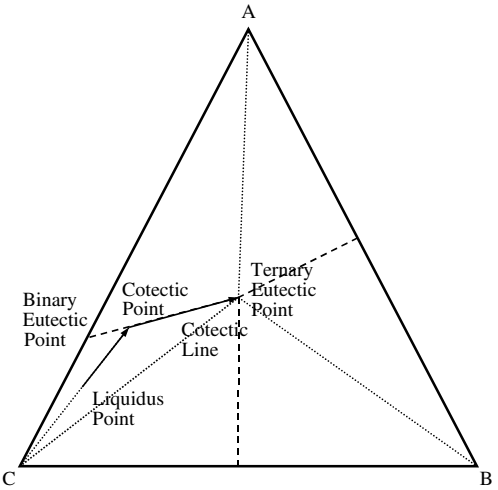

Fig. 2. Linearized ternary phase diagram.

surface is encountered and primary solidification of an C-rich α phase begins during equilibrium freezing of ternary alloy. The liquid line of descent (bold line) shows that the temperature and concentration evolve along the tie line until it reaches the cotectic point. At this point the liquid becomes saturated with a A-rich β solid solution and α, β phases solidify simultaneously. Further cooling causes the temperature and concentration of the residual liquid in the cotectic mush to evolve along the cotectic curve until the residual liquid reaches ternary eutectic concentrations. At this point the liquid becomes saturated with the solid solution δ. Cooling below the eutectic temperature causes the melt to transforms simultaneously into ternary eutectic α, β and δ phases. The liquidus surface associated with corner C is most naturally defined in terms of the compositions A and B as [16]

$$\theta = \theta_{\mathrm{m}} + m_{\ell}^{\mathrm{A}} f_{\ell}^{\mathrm{A}} + m_{\ell}^{\mathrm{B}} f_{\ell}^{\mathrm{B}} \tag{11}$$

where m_{ℓ}^{A} and m_{ℓ}^{B} are the dimensionless constant liquidus slopes that represent the variations of temperature with composition A and B, respectively. θ_{m} is dimensionless melting temperature of pure C substrate. The cotectic line extending from the C–A side of the ternary phase diagram can be represented as [16]

$$\theta = -m_{\mathrm{c}}^{\mathrm{A}}(f_{\ell}^{\mathrm{A}} - f_{\ell,\mathrm{be}}^{\mathrm{A}}) + \theta_{\mathrm{be}} = -m_{\mathrm{c}}^{\mathrm{B}} f_{\ell}^{\mathrm{B}} + \theta_{\mathrm{be}} \tag{12}$$

where $m_{\mathrm{c}}^{\mathrm{A}}$ and $m_{\mathrm{c}}^{\mathrm{B}}$ are constant slopes of the cotectic line that represent the variations of temperature with composition A and B, respectively. θ_{be} is the binary eutectic temperature at the C–A side. The liquidus and cotectic slopes can be expressed in terms of the above three coordinate points

$$m_{\mathrm{c}}^{\mathrm{A}} = \frac{1}{f_{\ell,\mathrm{te}}^{\mathrm{A}} - f_{\ell,\mathrm{be}}^{\mathrm{A}}}(\theta_{\mathrm{be}} - \theta_{\mathrm{te}}), \quad m_{\mathrm{c}}^{\mathrm{B}} = \frac{1}{f_{\ell,\mathrm{te}}^{\mathrm{B}}}(\theta_{\mathrm{be}} - \theta_{\mathrm{te}}) \tag{13}$$

$$m_{\ell}^{\mathrm{A}} = -\frac{1}{f_{\ell,\mathrm{be}}^{\mathrm{A}}}(\theta_{\mathrm{m}} - \theta_{\mathrm{be}}), \quad \frac{m_{\ell}^{\mathrm{A}}}{m_{\mathrm{c}}^{\mathrm{A}}} + \frac{m_{\ell}^{\mathrm{B}}}{m_{\mathrm{c}}^{\mathrm{B}}} = -1 \tag{14}$$

where θ_{te} denotes the ternary eutectic temperature. The equilibrium partition coefficients are

$$k_k^j = \frac{f_k^j}{f_{\ell}^j} \tag{15}$$

The superscript j denotes the components A and B, the subscript k denotes the solid phases of α, β, δ.

2.5. Primary solidification

The region in which one solid phase is in thermodynamic equilibrium with the liquid, $L \leftrightarrow \alpha$. The mixture enthalpy and species definitions and mass conservations of the molten splat and substrate are

$$\lambda_{\mathrm{m}} = f_{\ell}(Ste\theta + \lambda_{\ell}^0) + f_{\alpha} C_{ps\ell} Ste\theta \tag{16}$$

$$f_{\mathrm{m}}^j = f_{\alpha} f_{\alpha}^j + f_{\ell} f_{\ell}^j \tag{17}$$

$$f_{\alpha} + f_{\ell} = 1 \tag{18}$$

2.6. Secondary solidification

When the liquid composition reaches cotectic line, a second solid phase begins to precipitate and a three phase equilibrium is established, $L \leftrightarrow \alpha + \beta$. The mixture enthalpy and species definitions and mass conservations of the molten splat and substrate are rewritten as

$$\lambda_{\mathrm{m}} = f_{\ell}(Ste\theta + \lambda_{\ell}^0) + (f_{\alpha} + f_{\beta}) C_{ps\ell} Ste\theta \tag{19}$$

$$f_{\mathrm{m}}^j = f_{\alpha} f_{\alpha}^j + f_{\beta} f_{\beta}^j + f_{\ell} f_{\ell}^j \tag{20}$$

$$f_{\alpha} + f_{\beta} + f_{\ell} = 1 \tag{21}$$

The liquid compositions of components A and B along the cotectic line are, respectively, expressed as follows from Eq. (13)

$$f_{\ell}^{\mathrm{A}} = \frac{1}{m_{\mathrm{c}}^{\mathrm{A}}}(\theta_{\mathrm{be}} - \theta) + f_{\ell,\mathrm{be}}^{\mathrm{A}}, \quad f_{\ell}^{\mathrm{B}} = \frac{1}{m_{\mathrm{c}}^{\mathrm{B}}}(\theta_{\mathrm{be}} - \theta) \tag{22}$$

2.7. Eutectic solidification

When the liquid composition reaches a ternary eutectic point, a third solid phase begins to precipitate and a four phase equilibrium is established, $L \leftrightarrow \alpha + \beta + \delta$. The mixed relations for the ternary eutectic reaction are

$$\lambda_{\mathrm{m}} = f_{\ell}(Ste\theta_{\mathrm{te}} + \lambda_{\ell}^0) + (f_{\alpha} + f_{\beta} + f_{\delta}) C_{ps\ell} Ste\theta_{\mathrm{te}} \tag{23}$$

$$f_{\mathrm{m}}^j = f_{\alpha} f_{\alpha}^j + f_{\beta} f_{\beta}^j + f_{\delta} f_{\delta}^j + f_{\ell} f_{\ell}^j \tag{24}$$

$$f_{\alpha} + f_{\beta} + f_{\delta} + f_{\ell} = 1 \tag{25}$$

2.8. Temperature and enthalpy relationships

Equations for calculating phase fractions and compositions and temperature during the various stages of solidification.

(a) For enthalpy $\lambda_{\ell\mathrm{iq}} < \lambda_{\mathrm{m}}$,

$$\theta = \frac{1}{Ste}(\lambda_{\mathrm{m}} - \lambda_{\ell}^0), \quad f_{\ell} = 1 \tag{26}$$

The subscript ℓiq denotes the liquidus point and $f_{\ell}^j = f_{\mathrm{m}}^j$, where function

$$\lambda_{\ell\mathrm{iq}} = Ste\theta_{\ell\mathrm{iq}} + \lambda_{\ell}^0 \tag{27}$$

(b) For enthalpy $\lambda_{\mathrm{cp}} < \lambda_{\mathrm{m}} \leqslant \lambda_{\ell\mathrm{iq}}$,

$$f_{\alpha}^j = \left[\frac{k_{\alpha}^j}{1 + f_{\alpha}(k_{\alpha}^j - 1)}\right] f_{\mathrm{m}}^j, \quad f_{\ell}^j = \left[\frac{1}{1 + f_{\alpha}(k_{\alpha}^j - 1)}\right] f_{\mathrm{m}}^j \tag{28}$$

$$\theta = \frac{\lambda_{\mathrm{m}} - (1 - f_{\alpha})\lambda_{\ell}^0}{C_{ps\ell} Ste f_{\alpha} + (1 - f_{\alpha}) Ste} \tag{29}$$

The subscript cp denotes the cotectic point. Substituting f_{ℓ}^j from Eq. (28) in Eq. (11), f_{α} can be found from Eqs. (11) and (29) by bisection method. f_{ℓ} can be obtained from Eq. (18), where function

$$\lambda_{\mathrm{cp}} = f_{\ell,\mathrm{cp}}(Ste\theta_{\mathrm{cp}} + \lambda_{\ell}^0) + (1 - f_{\ell,\mathrm{cp}}) C_{ps\ell} Ste\theta_{\mathrm{cp}} \tag{30}$$

(c) For enthalpy $\lambda_{te} < \lambda_m \leqslant \lambda_{cp}$,

$$f_\alpha = \frac{\Lambda_1}{\Lambda_2}, \quad f_\ell = \frac{\frac{f_m^A}{f_\ell^A} - k_\beta^A - f_\alpha(k_\alpha^A - k_\beta^A)}{1 - k_\beta^A} \tag{31}$$

The subscript te denotes the ternary eutectic point. Substituting f_ℓ^A and f_ℓ^B from Eq. (22) in Eq. (31), respectively, θ can be found from Eqs. (19) and (31) by bisection method. f_ℓ^A and f_ℓ^B are calculated from Eq. (22), respectively. f_α^A, f_α^B, f_β^A and f_β^B can be obtained from Eq. (15). f_β is calculated from Eq. (21), where functions

$$\lambda_{te} = f_{\ell,te}(Ste\theta_{te} + \lambda_\ell^0) + (1 - f_{\ell,te})C_{ps\ell}Ste\theta_{te} \tag{32}$$

$$\Lambda_1 = \frac{f_m^A}{f_\ell^A}(1 - k_\beta^B) - \frac{f_m^B}{f_\ell^B}(1 - k_\beta^A) - k_\beta^A + k_\beta^B \tag{33}$$

$$\Lambda_2 = k_\alpha^A - k_\beta^A - k_\alpha^A k_\beta^B - k_\alpha^B + k_\beta^B + k_\beta^A k_\alpha^B \tag{34}$$

(d) For enthalpy $\lambda_{so\ell} < \lambda_m \leqslant \lambda_{te}$,

$$f_\ell = \frac{\lambda_m - C_{ps\ell}Ste\theta_{te}}{Ste\theta_{te} + \lambda_\ell^0 - C_{ps\ell}Ste\theta_{te}} \tag{35}$$

$$f_\alpha = \frac{\Lambda_3}{\Lambda_4}, \quad f_\beta = \frac{\frac{f_m^A}{f_{\ell,te}^A} - f_\alpha(k_\alpha^A - k_\delta^A) - k_\delta^A - f_\ell(1 - k_\delta^A)}{k_\beta^A - k_\delta^A} \tag{36}$$

The subscript soℓ denotes the solidus point. $f_{\ell,te}^A$, $f_{\ell,te}^B$ and θ_{te} are given from ternary phase diagram. f_α^A, f_α^B, f_β^A, f_β^B, f_δ^A and f_δ^B can be obtained from Eq. (15). f_δ is calculated from Eq. (25), where functions

$$\lambda_{so\ell} = SteC_{ps\ell}\theta_{so\ell} \tag{37}$$

$$\Lambda_3 = \left(\frac{f_m^A}{f_{\ell,te}^A} - f_\ell\right)(k_\beta^B - k_\delta^B) - \left(\frac{f_m^B}{f_{\ell,te}^B} - f_\ell\right)(k_\beta^A - k_\delta^A) + (k_\delta^B k_\beta^A - k_\delta^A k_\beta^B)(1 - f_\ell) \tag{38}$$

$$\Lambda_4 = k_\alpha^A k_\beta^B - k_\delta^A k_\beta^B - k_\alpha^A k_\delta^B - k_\alpha^B k_\beta^A + k_\delta^B k_\beta^A + k_\alpha^B k_\delta^A \tag{39}$$

(e) For enthalpy $\lambda_m \leqslant \lambda_{so\ell}$,

$$\theta = \frac{\lambda_m}{SteC_{ps\ell}}, \quad f_\ell = 0 \tag{40}$$

$f_\alpha^A, f_\alpha^B, f_\beta^A, f_\beta^B, f_\delta^A, f_\delta^B, f_\alpha, f_\beta, f_\delta$ can be obtained from the above-mentioned procedure by setting $f_\ell = 0$.

2.9. Determine the solidus temperature and solidification path

The value of the solidus temperature, $\theta_{so\ell}$, is needed to find the temperature from the mixture enthalpy and a determination must be made of the region in which solidification is occurring. The first step in determining $\theta_{so\ell}$ is to find out in which region of the phase diagram (primary, cotectic, or eutectic point) solidification ends. At the transition point between primary and cotectic solidification, $f_\beta = 0$ and the phase compositions and fractions can be calculated from Eqs. (12), (15), (17) and (18). If the liquid fraction calculated at this point, $f_{\ell,cp}$ is less than zero, solidification ends with only α phase formation. The solidus temperature can then be found by using $f_\alpha = 1$ and $f_m^i = f_\alpha^i$ with Eqs. (11) and (15). If $f_{\ell,cp} > 0$, some liquid survives to freeze along the cotectic line. Next, determining the residual liquid fraction before the third solid phase begins to form. At the eutectic point, the eutectic temperature and liquid composition are known, between cotectic solidification and eutectic reaction, $f_\delta = 0$ and the phase compositions and fractions can be calculated from Eqs. (15), (20) and (21). If $f_{\ell,te} < 0$, freezing is complete somewhere along the cotectic line. The $\theta_{so\ell}$ can be determined from Eqs. (15), (20), (21) and (22) with $f_\ell = 0$, which are solved simultaneously. If there is liquid left at the beginning of the eutectic reaction $f_{\ell,te} > 0$, $\theta_{so\ell} = \theta_{te}$, which is known from the phase diagram [20].

2.10. Numerical method

A successive relaxation method with a relaxation factor 0.9 was used for the energy and species transport equations in the numerical scheme. The grid system is in uniform spaces in the splat and substrate, respectively. In testing different grid systems, use of the grid system 200×200 for the splat and substrate, respectively, is quite good to obtain solutions independent of the variation in meshes. The solution procedure was as follows:

1. Specify initial and working conditions, and properties of the splat and substrate.
2. Determine the solidus temperature and solidification path.
3. Determine temperature, phase fractions and compositions.
4. Solve energy and species Eqs. (1) and (2) for splat and substrate together with boundary conditions, respectively.
5. Check convergence of enthalpy, species and total energy balance of the splat and substrate and to relative errors less than 10^{-5}, and 10^{-3}, respectively. Otherwise, go to step 2.
6. Go to step 2 for the next time if time is less than the setting time.

3. Results and discussion

To confirm relevancy and accuracy of this model, comparisons between the predicted and measured thicknesses of primary, cotectic and eutectic mushy fronts as functions of time [23] for a ternary alloy H_2O–KNO_3–$NaNO_3$ solidified from a cooled boundary are shown in Fig. 3. In this case, the referenced data for comparison are listed in Table 1. The predicted thicknesses of cotectic and eutectic mushy fronts as functions of time agree quite well with the experimental data [23] by choosing

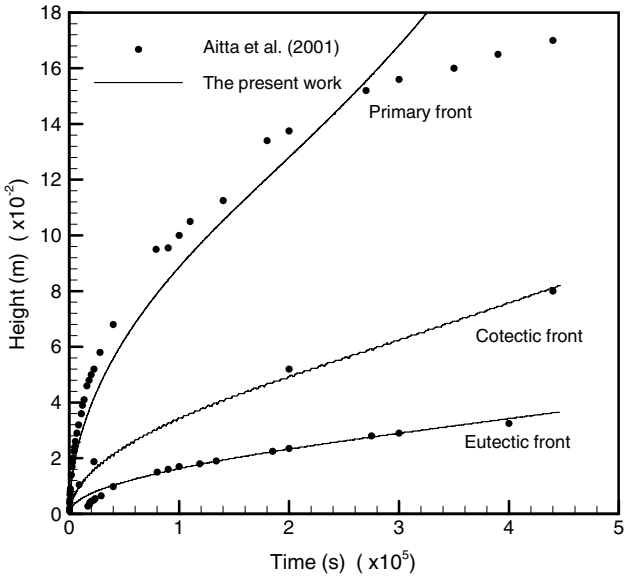

Fig. 3. Comparisons of predicted dimensional thicknesses of primary, cotectic and eutectic mushy fronts in the splat versus dimensional time between this work and the results from Aitta et al. [23].

Table 1
Values of the data for comparison with experimental data [23]

$c_{p\ell}$	2 kJ/kg K
c_{ps}	4.2 kJ/kg K
k_ℓ	0.65 W/m K
k_s	1.88 W/m K
ρ_s,ρ_ℓ	1000 kg/m^3
h_f	334 kJ/kg
T_0	293 K
T_{be}	268 K
T_{te}	246 K
T_m	276 K
T_∞	150 K
s	0.33 m
D_ℓ^A	4.89×10^{-10} m^2/s
$f_{m,0}^A$	0.035 wt%
$f_{m,0}^B$	0.152 wt%
$f_{\ell,be}^A$	0.1 wt%
$f_{\ell,te}^A$	0.06 wt%
$f_{\ell,te}^B$	0.37 wt%
k_α^A	0.0001
k_α^B	0.0001
k_β^A	1.0
k_β^B	0.0001
k_δ^A	0.0001
k_δ^B	1.0

$$h_\infty = 9.8 \times 10^5 – 1.89 \times 10^6 (\tilde{\delta}_p)^{1/2} \quad \mathrm{W/m^2\,K},$$
$$k_m = 1.88 \times (f_\alpha + 10^{-3} f_\beta + 10^{-4} f_\delta) + 0.65 f_\ell \quad \mathrm{W/m\,K}$$

$\tilde{\delta}_p$ is the dimensional thickness of primary mushy front in the splat. The deviation in the predicted thickness of the primary mushy front has become higher than in the experimental data after 2.7×10^5 s. This may be due to; the increased thicknesses of the various mushy layers, the thermal conductivities of different precipitated solid phases, or the heat transfer coefficient at the bottom of the splat, which are variable during the solidification process.

When the molten ternary alloy splat contacts with the ternary eutectic solid substrate the results are a melting of the top surface of the substrate, and a solidifying at the bottom of the splat. It is interesting to observe the variations of the phase fraction distributions during the solidification process of the splat. Fig. 4 shows the phase fraction distributions in the splat for different dimensionless solidification times. The results are referred to as the dimensionless parameters presented in Table 2. It can be seen that at $\tau = 4 \times 10^{-4}$, the cotectic mushy layer (α and β phases precipitate in the melt) forms at the bottom surface of the splat, while the top surface remains in liquid phase, the zone between the two regions is called the primary mushy layer (only α phase precipitates in the melt). The primary and cotectic mushy fronts grow to the top surface while the heat flux continues to transfer from the splat to the substrate. At $\tau = 1 \times 10^{-3}$, the bottom of the splat has completely solidified, this is called the ternary eutectic solid (It consists of α, β and δ solid phases), followed by the ternary eutectic mushy (α, β and δ phases precipitate in the melt), then the cotectic mushy and finally the primary mushy layer. The dimensionless thicknesses of these mushy layers are about 0.44, 0.01, 0.28 and 0.26, respectively. In a comparison between $\tau = 6 \times 10^{-4}$ and 1×10^{-3}, the thicknesses of the eutectic solid and the cotectic mushy layers increase with dimensionless time, as the eutectic and primary mushy layers decrease. The phase fraction distributions in the substrate for different dimensionless times, are shown in Fig. 5. The thicknesses of the molten and eutectic mushy layers are about 0.24 and 0.04 at $\tau = 2 \times 10^{-4}$, respectively. It is noted that the thickness

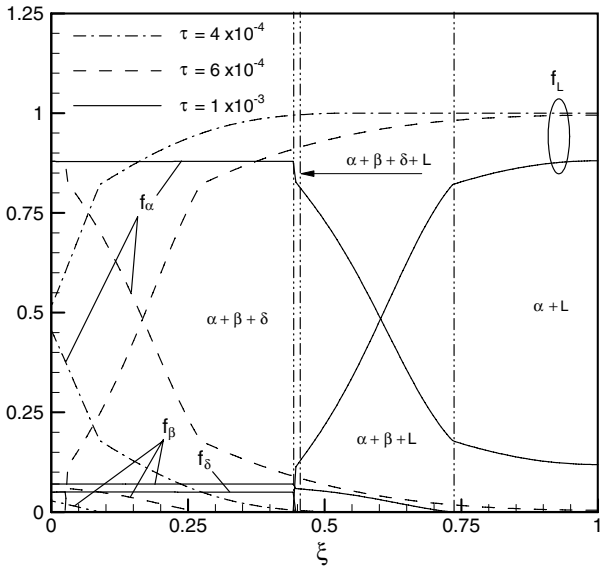

Fig. 4. Phase fraction distributions in the splat for different dimensionless times, $\tau = 4 \times 10^{-4}$, 6×10^{-4}, 1×10^{-3}; the dimensionless parameters are based on Table 2.

Table 2
Typical values of the independent dimensionless parameters

$Bi_{2,\infty}$	0.5
Bi_c	10
$K_{s\ell}$	1.2
$C_{ps\ell}$	1.2
Ste	0.8
$\theta_{1,0}$	3.0
$\theta_{2,0}$	1.0
θ_{be}	1.65
θ_{te}	1.61
θ_m	1.7
$f^A_{\ell,be}$	1.02
$f^A_{\ell,te}$	1.3
$f^B_{\ell,te}$	0.36
$f^B_{1,m,0}$	0.136
$f^A_{2,m,0}$	1.3
$f^B_{2,m,0}$	0.36
k^A_α	0.31
k^B_α	0.30
k^A_β	6.76
k^B_β	0.296
k^A_δ	0.39
k^B_δ	1.85
S	1
Le	8×10^3

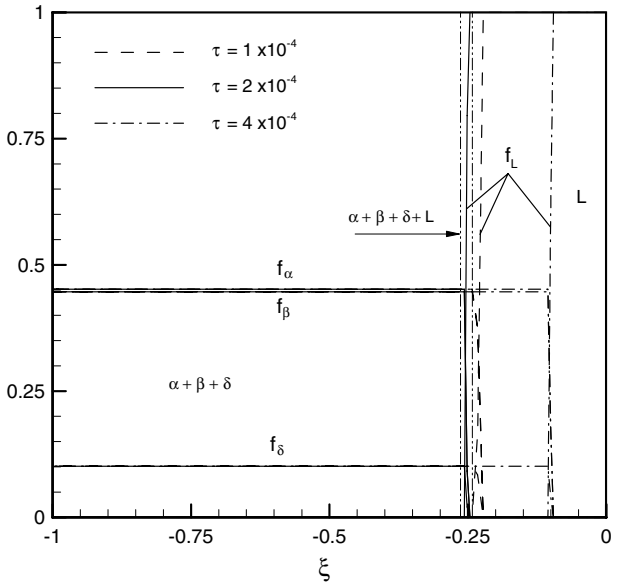

Fig. 5. Phase fraction distributions in the substrate for different dimensionless times, $\tau = 1 \times 10^{-4}$, 2×10^{-4}, 4×10^{-4}; the dimensionless parameters are based on Table 2.

of the molten layer first increases then later decreases from $\tau = 1 \times 10^{-4}$–4×10^{-4}, this represents the heat flux being removed by the substrate, which is more than the heat flux being transferred into the substrate at $\tau = 4 \times 10^{-4}$. So that the melting interface moves downward until it reaches the maximum melting depth then moves upward. The re-solidification process of the substrate has begun at $\tau = 4 \times 10^{-4}$. (This can be seen in Fig. 8.)

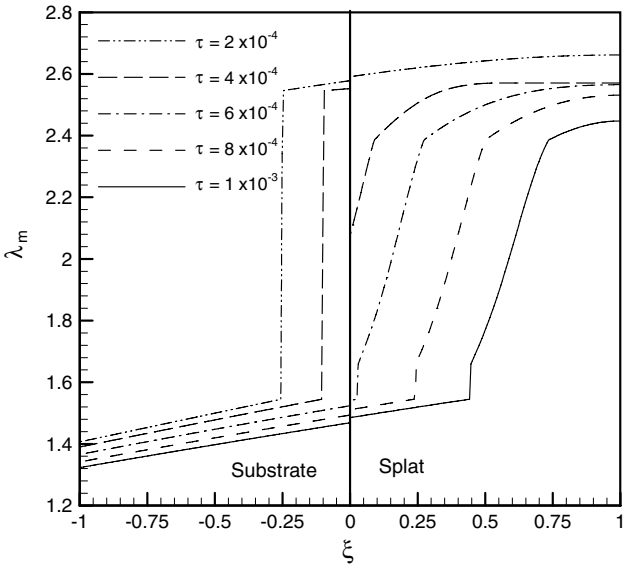

Fig. 6. Dimensionless enthalpy profiles in the splat and the substrate for different dimensionless times, $\tau = 2 \times 10^{-4}$, 4×10^{-4}, 6×10^{-4}, 8×10^{-4}, 1×10^{-3}; the dimensionless parameters are based on Table 2.

Dimensionless enthalpy profiles in the splat and the substrate for different dimensionless times are presented in Fig. 6. At $\tau = 2 \times 10^{-4}$, the top surface of the substrate has melted and the bottom of the splat remains in liquid phase. So the difference of enthalpy across the interface between the splat and the substrate is small. The bottom of the splat has precipitated α, β solid phases at $\tau = 4 \times 10^{-4}$ (see Fig. 4), therefore, the gap of enthalpy across the interface is large, and the enthalpy of the substrate is larger than that of the splat which results from the latent heat of fusion that exists. The gap becomes smaller at $\tau = 6 \times 10^{-4}$ because of the top surface of the substrate has completely re-solidified (see Fig. 8). In these dimensionless enthalpy profiles in the splat exist some discontinued points, resulting from the different solid phases precipitated. (This can be seen in Fig. 4.) The dimensionless top and bottom surface temperatures of the splat and the substrate change with time while the molten ternary alloy splat contacts with the ternary eutectic solid substrate, these are shown in Fig. 7. At the initial stage, the top and bottom surface temperatures of the splat and the substrate rapidly decrease and increase, respectively. The top surface temperature evolution of the substrate exists a drop at $\tau = 5.3 \times 10^{-4}$, this results from the substrate that has completely re-solidified (see Fig. 8), which is due to the thermal conductivity of the solid being larger than the liquid ($K_{s\ell} = 1.2$). The heat flux at the interface between the splat and the substrate is removed by the substrate, which is increasing while the top surface temperature is decreasing. Hence, the difference of temperature across the interface is larger.

The growths of the primary, cotectic and eutectic fronts in the solidified splat and melted re-solidified substrate versus dimensionless time are affected by processing

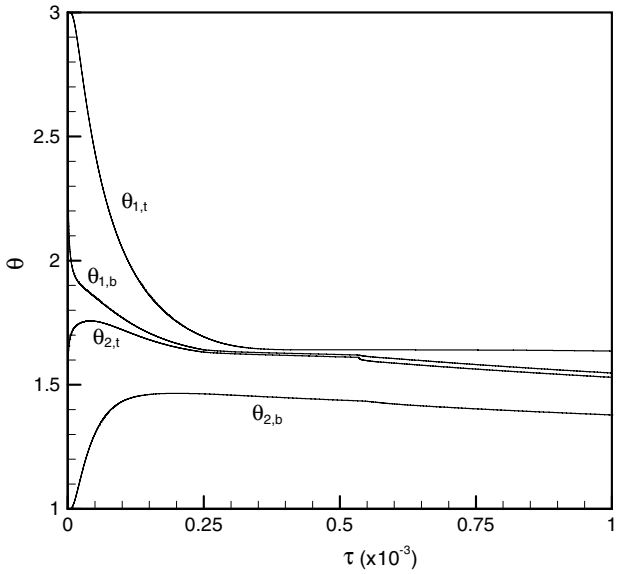

Fig. 7. Dimensionless temperatures of the top and bottom surfaces of the splat and the substrate as functions of dimensionless time; the dimensionless parameters are based on Table 2.

parameters presented in Fig. 8(a)–(e). It should be noted that the solid line is first discussed and refers to the dimensionless parameters presented in Table 2. All of the other lines are obtained by applying data of the dimensionless parameters from Table 2, excluding the specified parameter having the value in this figure. The positive and negative values of the ordinate represent locations of the different mushy fronts in the splat and the substrate, respectively. The primary front (δ_P) separates the liquid from the primary mushy layer, which is defined as the position of α solid phase precipitated by interpolation of the liquid and the primary mushy layers. The eutectic front (δ_E) separates the eutectic solid from the eutectic mushy layer, which is defined as the position of $f_\ell = 0$. The cotectic front (δ_C) located between the primary and cotectic mushy layers is defined as the position of β solid phase precipitated. The mushy zone in the splat consists of the primary, cotectic, and eutectic mushy layers. In contrast with the splat, only the eutectic mushy layer exists during melting and re-solidifying of the substrate because it possesses ternary eutectic compositions. The thickness of the ternary eutectic mushy layer is very narrow in this study, (This can be seen in Figs. 4 and 5.) hence the eutectic mushy layers in the splat and the substrate are represented with lines (resulting from interpolation). The substrate begins to melt while it contacts the higher temperature of the splat, and the melting front of the substrate begins to move in the negative ξ coordinate direction. The dimensionless melted thickness of the substrate increases with time until it has reached a maximum value of about 0.26 at $\tau = 0.16$, then it decreases until re-solidification is completed at $\tau = 0.54$. Initially, the onset time for the α solid phase to precipitate in the splat is about $\tau = 0.25$ (based on δ_P) and the cotectic front δ_C begins to grow at $\tau = 0.3$, δ_P moves in the positive ξ coordinate direction until it reaches the top surface at $\tau = 0.44$. At this time, the splat consists of the primary and cotectic mushy layers. At $\tau = 0.57$, the eutectic solid has now formed at the bottom surface of the splat and the eutectic front is growing in an upward direction. It is worth noting that the δ_C curve has a discontinued point, which results from the eutectic solid precipitates at the bottom of the splat. Here the growth rate of δ_P is parabolic, and both δ_C and δ_E are linear. It can also be noted that the contact conditions of the interface between the splat and the substrate can be separated by (a) the liquid melted from the substrate which contacts with the liquid of the splat from $\tau = 0.002$–0.25, and (b) from $\tau = 0.25$–0.54 the liquid substrate contacts the mushy zone of the splat, (c) the re-solidified substrate contacts the mushy zone of the splat from $\tau = 0.54$–0.57, and (d) at $\tau = 0.57$, the re-solidified substrate contacts the solidified splat.

As the contact Biot number increases ($Bi_c = 10$–100), it represents the contact thermal resistant, which decreases while the heat flux increases across the interface between the splat and the substrate. This results in increasing the maximum melted depth and the time for the complete re-solidification of the substrate. The onset times for initial growth of δ_P and δ_C are shortened, as shown in Fig. 8(a). A decrease in the Lewis number ($Le = 8 \times 10^3$–7×10^3) represents a decrease of thermal diffusivity coefficient of liquid, which results in a reduction of the heat conduction flux from the liquid splat to the solid substrate. Hence, the times for reaching the maximum melted depth and the complete re-solidification of the substrate are delayed. The initial growth times for δ_P, δ_C and δ_E in the splat are all increased. An increase in the dimensionless thickness of the substrate enhances the cooling effects of the heat flux being removed from the interface between the splat and the substrate by it ($S = 1$–5). The thicker the substrate, the quicker the heat flux will be removed by the substrate. The maximum melted depth and the complete re-solidification time of the substrate, and the initial growth times for δ_P, δ_C and δ_E in the splat are all shortened.

As shown in Fig. 8(b), as the solid-to-liquid specific heat ratio decreases ($C_{psl} = 1.2$–1.0), the maximum melted thickness and the complete re-solidification time of the substrate increase. This is because of a lower value of the specific heat ratio implies that the energy required to change the temperature of the solid substrate is smaller. The initial growth times are increased for δ_P, δ_C and δ_E in the splat and this is due to the thermal conductivity of the liquid being smaller than the solid ($K_{s\ell} = 1.2$). Decreasing the solid-to-liquid thermal conductivity ratio ($K_{s\ell} = 1.2$–0.8) will delay the initial growth times for δ_P, δ_C and δ_E in the splat, and will increase the maximum melted thickness and re-solidification time of the substrate. This is a result of reducing the heat dissipated through the solid substrate to its surroundings. A decrease in the Stefan number ($Ste = 0.8$–0.4) represents an increase in the latent heat of fusion. Physically speaking, the time required for a phase change increases if the latent heat is large. Therefore, the

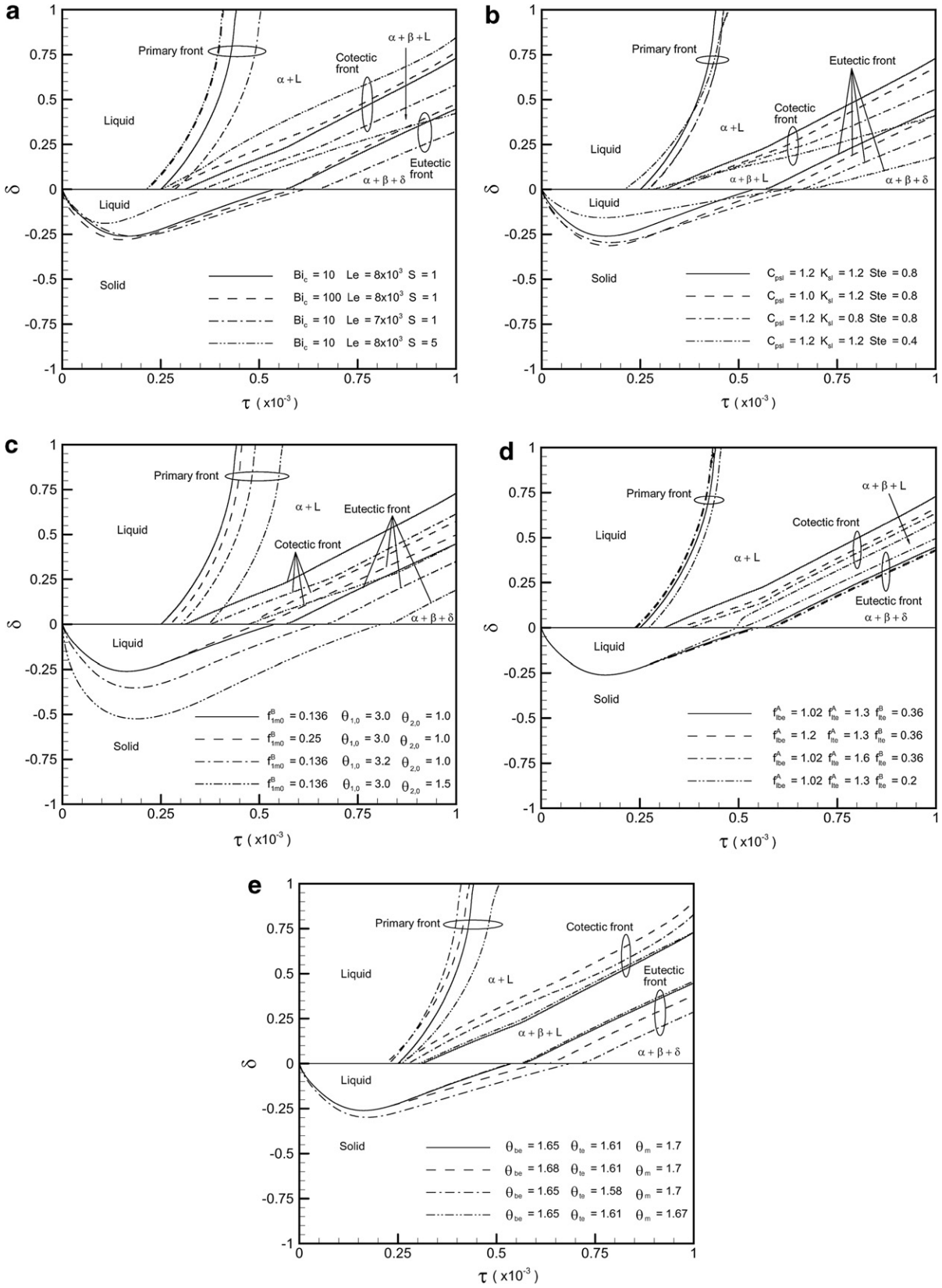

Fig. 8. Dimensionless thicknesses of the primary, cotectic and eutectic fronts in the splat and eutectic front in the substrate versus dimensionless time are affected by (a) the contact Biot number, Lewis number and the dimensionless thickness of the substrate; (b) solid-to-liquid specific heat ratios, solid-to-liquid thermal conductivity ratios and the Stefan number; (c) dimensionless initial solute content of B in the splat, and initial temperatures of the splat and the substrate; (d) dimensionless solute content of A at binary eutectic point, A and B solute contents at the ternary eutectic point; (e) dimensionless binary eutectic, ternary eutectic and the melting temperatures; solid line is based on Table 2.

maximum melted depth and the complete re-solidification time of the substrate decreases and increases, respectively. The former results in shortening the initial growth times for δ_P and δ_C, the latter results in a delay for δ_E in the splat.

Both Fig. 2 and Fig. 8(c) show that an increase in the dimensionless initial B solute concentration in the splat ($f^B_{1,m,0} = 0.136$–0.25) represents the liquidus point which is closer to the ternary eutectic point and it decreases the temperatures at the liquidus and the cotectic points. Hence, the onset times for δ_P and δ_C are delayed, and the thickness of the cotectic mushy layer is reduced. Respectively, the maximum melted thickness of the substrate is unchanged, but the complete re-solidification time is reduced. The latter results in a reduction of the onset time for δ_E. Increasing the dimensionless initial temperatures of the splat and the substrate ($\theta_{1,0} = 3.0$–3.2 and $\theta_{2,0} = 1.0$–1.5) result in increasing the maximum melted thickness and the complete re-solidification time of the substrate. This is because of the higher the initial temperature of the splat, the more heat flux will be transferred from the splat into the substrate. On the other part, the higher the initial temperature of the substrate, the less heat flux is required to melt the substrate. Increasing the initial temperatures of the splat and the substrate represent the onset time for the freezing of the splat will increase and the ability of the substrate to cool the splat will decrease, respectively. Hence, the onset times for δ_P, δ_C and δ_E will be delayed.

Increasing the A solute concentrations at the binary and ternary eutectic points ($f^A_{\ell,be} = 1.02$–1.2 and $f^A_{\ell,te} = 1.3$–1.6) will result in increasing the temperature at the liquidus point and decreasing the temperature at the cotectic point. [This can be seen in Eqs. (11), (13) and (14).] The former results in decreasing the onset time for δ_P and the latter results in increasing the onset time for δ_C, as well as an increase in the thickness of the primary mushy layer. The complete re-solidification time of the substrate and the onset time for δ_E will both be delayed. Decreasing the B solute concentration at the ternary eutectic point ($f^B_{\ell,te} = 0.36$–0.2) results in increasing both the liquidus and cotectic slopes of the B solute. Hence, the liquidus and the cotectic point temperatures are reduced and the onset times for δ_P and δ_C are delayed. The complete re-solidification time of the substrate and the onset time for δ_E will be shortened. Therefore, the thickness of the cotectic mushy layer will be reduced.

Increasing the binary eutectic temperature ($\theta_{be} = 1.65$–1.68) increases the slopes of both cotectic lines of the A and B solutes [see Eq. (13)] and decreases the slope of the liquidus line of the A solute. This results in increasing the liquidus point temperature and decreasing the onset times for δ_P and δ_C, which are shown in Fig. 8(e). Decreasing the ternary eutectic temperature ($\theta_{te} = 1.61$–1.58) results in increasing the slope of the liquidus line of B solute, and decreasing the liquidus point temperature. However the dimensionless melted thickness of the substrate will increase. This requires more heat flux to melt it which results in a shortening of the onset times for δ_P and δ_C. The complete re-solidification time of the substrate and the onset time for δ_E will both be delayed. The thickness of the cotectic mushy zone increases with increasing the binary and decreasing the ternary eutectic temperatures. Decreasing the dimensionless melting temperature of pure C metal ($\theta_m = 1.7$–1.67) represents a decrease in the liquidus point temperature, which therefore delays the onset time for δ_P.

4. Conclusion

This study self-consistently and extensively investigates the solidification of the ternary alloy liquid splat, and the heating, melting and re-solidification of the ternary eutectic solid substrate are affected by different dimensionless parameters and thermal physical properties of the material. A splat may induce the substrate to melt and is an important consideration in many manufacturing processes, such as spray deposition, casting, and microcasting. A strong bond is needed via the melting of the substrate. This work therefore provides quantitative results applicable to control the solidification of the splat, and the melting and re-solidification of the substrate related to strong bonding. To control the freezing and melting of a splat and substrate, respectively, dimensionless independent parameters can be appropriately selected. Results of this study are compared with experimental data provided by Aitta et al. The growth rates of the cotectic and eutectic fronts are found to agree well with the experimental data. The effects of the initial solute concentrations in the liquid layer, solute concentrations and temperatures at the binary and ternary eutectic points on the thicknesses of the different mushy layers are important and presented.

References

[1] M.C. Flemings, Solidification Processing, McGraw-Hill, Inc., 1974.
[2] W. Kurz, D.J. Fisher, Fundamentals of Solidification, Trans. Tech. Publications, 1989.
[3] S.R. Coriell, G.B. McFadden, R.F. Sekerka, W.J. Boettinger, Multiple similarity solutions for solidification and melting, J. Crystal Growth 191 (1998) 573–585.
[4] L. Nastac, Analytical modeling of solute redistribution during the initial unsteady unidirectional solidification of binary dilute alloys, J. Crystal Growth 193 (1998) 271–284.
[5] S. Chakraborty, P. Dutta, An analytical solution for conduction-dominated unidirectional solidification of binary mixtures, Appl. Math. Model. 26 (2002) 545–561.
[6] M.J.M. Krane, F.P. Incropera, A scaling analysis of the unidirectional solidification of a binary alloy, Int. J. Heat Mass Transfer 39 (17) (1996) 3567–3579.
[7] W.D. Bennon, F.P. Incropera, A continuum model for momentum, heat and species transport in binary solid–liquid phase change systems—I. Model formulation, Int. J. Heat Mass Transfer 30 (10) (1987) 2161–2170.
[8] M.E. Ganaoui, P. Bontoux, A. Lamazouade, E. Leonardi, G.D.V. Davis, Computational model for solutal convection during directional solidification, Numer. Heat Transfer B 41 (2002) 325–338.
[9] D. Celentano, M. Cruchaga, N. Moraga, J. Fuentes, Modeling natural convection with solidification in mould cavities, Numer. Heat Transfer A 39 (2001) 631–654.

[10] A. Teskeredžić, I. Demirdžić, S. Muzaferija, Numerical method for heat transfer, fluid flow, and stress analysis in phase-change problems, Numer. Heat Transfer B 42 (2002) 437–459.
[11] S. Chakraborty, P. Dutta, Effects of solutal undercooling on three-dimensional double-diffusive convection and macrosegregation during solidification of a binary alloy, Numer. Heat Transfer A 48 (2005) 261–281.
[12] R. Mehrabian, M.C. Flemings, Macrosegregation in ternary alloys, Metall. Trans. 1 (1970) 455–464.
[13] S.W. Chen, Y.A. Chang, Microsegregation in solidification for ternary alloys, Metall. Trans. A 23A (1992) 1038–1043.
[14] V.R. Voller, A similarity solution for the solidification of a multicomponent alloy, Int. J. Heat Mass Transfer 40 (12) (1997) 2869–2877.
[15] S.A. Cefalu, M.J.M. Krane, Microsegregation in open and closed multicomponent systems, Mater. Sci. Eng. A 359 (2003) 91–99.
[16] D.M. Anderson, A model for diffusion-controlled solidification of ternary alloys in mushy layers, J. Fluid Mech. 483 (2003) 165–197.
[17] M.C. Schneider, C. Beckermann, Formation of macrosegregation by multicomponent thermosolutal convection during the solidification of steel, Metall. Mater. Trans. A 26A (1995) 2373–2388.
[18] C. Beckermann, R. Viskanta, Mathematical modeling of transport phenomena during alloy solidification, Appl. Mech. Rev. 46 (1993) 1–27.
[19] C.R. Swaminathan, V.R. Voller, Towards a general numerical scheme for solidification systems, Int. J. Heat Mass Transfer 40 (12) (1997) 2859–2868.
[20] M.J.M. Krane, F.P. Incropera, D.R. Gaskell, Solidification of ternary metal alloys—I. Model development, Int. J. Heat Mass Transfer 40 (16) (1997) 3827–3835.
[21] M.J.M. Krane, F.P. Incropera, Solidification of ternary metal alloys—II. Predictions of convective phenomena and solidification behavior in Pb–Sb–Sn alloys, Int. J. Heat Mass Transfer 40 (16) (1997) 3837–3847.
[22] M.J.M. Krane, F.P. Incropera, D.R. Gaskell, Solidification of a ternary metal alloy: a comparison of experimental measurements and model predictions in a Pb–Sb–Sn system, Metall. Mater. Trans. A 29A (1998) 843–853.
[23] A. Aitta, H.E. Huppert, M.G. Worster, Diffusion-controlled solidification of a ternary melt from a cooled boundary, J. Fluid Mech. 432 (2001) 201–217.
[24] A.F. Thompson, H.E. Huppert, M.G. Worster, A. Aitta, solidification and compositional convection of a ternary alloy, J. Fluid Mech. 497 (2003) 167–199.
[25] J.H. Zaat, A quarter of a century of plasma spraying, Annu. Rev. Mater. Sci. 13 (1983) 9–42.
[26] H.-D. Steffens, B. Wielage, J. Drozak, Interface phenomena and bonding mechanism of thermally-sprayed metal and ceramic composites, Surf. Coat. Technol. 45 (1–3) (1991) 299–308.
[27] C.H. Amon, K.S. Schmaltz, R. Merz, F.B. Prinz, Numerical and experimental investigation of interface bonding via substrate remelting of an impinging molten metal droplet, ASME J. Heat Transfer 118 (1996) 164–172.
[28] B. Kang, J. Waldvogel, D. Poulikakos, Remelting phenomena in the process of splat solidification, J. Mater. Sci. 30 (19) (1995) 4912–4925.
[29] S.P. Wang, G.X. Wang, E.F. Matthys, Melting and resolidification of a substrate in contact with a molten metal: operational maps, Int. J. Heat Mass Transfer 41 (10) (1998) 1177–1188.
[30] L. Li, X.Y. Wang, G. Wei, A. Vaidya, H. Zhang, S. Sampath, Substrate melting during thermal spray splat quenching, Thin Solid Films 468 (2004) 113–119.
[31] F.B. Yeh, P.S. Wei, S.H. Chiu, Distinct property effects on rapid solidification of a thin liquid layer on a substrate subject to self-consistent melting, J. Crystal Growth 247 (2003) 563–575.
[32] P.S. Wei, F.B. Yeh, Heat Transfer coefficient in rapid solidification of a liquid layer on a substrate, ASME J. Heat Transfer 122 (2000) 792–800.